ADVANCED FUNCTIONAL MATERIALS
www.afm-journal.de

Covalently-Bonded Diaphite Nanoplatelet with Engineered Electronic Properties of Diamond

Zhaofeng Zhai, Chuyan Zhang, Bin Chen, Ying Xiong, Yan Liang, Lusheng Liu, Bing Yang, Nianjun Yang, Xin Jiang, and Nan Huang**

Diamond, as a highly promising "extreme" semiconductor material, necessitates electronic property engineering to unleash its full potential in electronic and photonic devices. In this work, the diaphite nanoplatelet, consisting of (1$\bar{1}$1) planes of diamond nanoplatelet covalently bonded with graphite (0001) planes, is facilely synthesized using one-step microwave plasma enhanced chemical vapor deposition method. The high-energy plasma created by the pillar plays a crucial role in the formation. Importantly, altered electronic and optical properties are determined in the diaphite nanoplatelet through electron energy loss spectrum, density functional theory calculations, and cathodoluminescence spectroscopy. It is revealed that the strong sp^3/sp^2-hybridized interfacial covalent bonding in the diaphite nanoplatelet induces the electron transfer from diamond to graphite. This modulates the electronic structure of the near-interface layer of diamond and triggers a new local trapping band below the conduction band minimum within the bandgap. Consequently, the covalently-bonded diaphite exhibits a different optical emission characteristic ranging from 2.5 to 3.64 eV, featuring a significant peak blueshift of 430 meV compared to the H-terminated diamond. This work demonstrates a novel method to engineer the electronic properties of diamond, opening avenues for functional semiconductor device applications of diamond.

1. Introduction

Diamond, featuring wide bandgap, high thermal conductivity, high breakdown field strength, and high carrier mobility, has been regarded as an "extreme" semiconductor for applications in electronic and photonic devices operated in harsh conditions (e.g., high-power diodes, high-frequency field-effect transistor, and robust solar-bind photodetector).[1,2] Nevertheless, a significant challenge that has baffled material researchers for a few decades in the construction of diamond semiconductor devices is the efficiently engineering of the electronic property. Atomic doping of impurity (e.g., B, N, and P) is the most common route to tune the electronic band structure,[3] but it still encounters the hardship of low solubility of dopants and the degradation of diamond crystallinity if heavily doping.[4,5] Strain engineering is another potent pathway to manipulate electronic properties.[1,6] However, preserving large strain in diamond is a formidable obstacle that must be addressed before the practical application.[7] Therefore, there is still tremendous interest in exploring a novel method for engineering the electronic properties of diamonds.

Recently, gradia,[8] or diaphite,[9,10] named for the analogous structure to diamond and graphite, arouses increasing attentions. Such a new carbon crystalline allotrope composed of sp^3-hybridized diamond and

Z. Zhai, C. Zhang, B. Chen, Y. Liang, L. Liu, B. Yang, X. Jiang, N. Huang
Shenyang National Laboratory for Materials Science (SYNL)
Institute of Metal Research (IMR)
Chinese Academy of Sciences (CAS)
No.72 Wenhua Road, Shenyang 110016, China
E-mail: xin.jiang@uni-siegen.de; nhuang@imr.ac.cn

Z. Zhai, B. Chen, B. Yang, N. Huang
School of Materials Science and Engineering
University of Science and Technology of China
No.72 Wenhua Road, Shenyang 110016, China

Y. Xiong
State Key Laboratory for Environment-Friendly Energy Materials
Southwest University of Science and Technology
Mianyang 621010, China

N. Yang
Department of Chemistry & IMO-IMOMEC
Hasselt University
Diepenbeek 3590, Belgium

X. Jiang
Institute of Materials Engineering
University of Siegen
No.9-11 Paul-Bonatz-Str., 57076 Siegen, Germany

The ORCID identification number(s) for the author(s) of this article can be found under https://doi.org/10.1002/adfm.202401949

DOI: 10.1002/adfm.202401949

sp^2-hybridized graphite nanodomains is expected to combine the characteristics of both parties, exhibiting distinctive mechanical, electronic, and thermal properties.[11,12] For example, Tian et al. demonstrated the diaphite consisting of diamond and graphite covalently bonded to each other possesses excellent toughness, ultrahigh hardness (51 GPa), and high electrical conductivity (8×10^{-4} Ω·m).[8] More intriguingly, the strength of covalent bonds at the diamond/graphite interface was calculated to be ≈150 GPa, even surpassing that of graphene.[13] Such intensive interfacial interaction could induce fascinating modulation of electronic properties. For instance, a significant reduction of the bandgap as large as 4.1 eV was experimentally observed at the AlN/Al_2O_3 interface when contrasting with the bulk, due to the strong N—Al—O bonds across the interface.[14] Meanwhile, it is verified that the H-covalently terminated diamond results in a significant surface energy band bending.[15] These imply that the diamond covalently bonded with graphite, namely, diaphite, may possess distinctly varied electronic properties compared to pristine diamond, which, however, have rarely been experimentally reported or investigated before.

One possible reason lies in the challenge of preparing nanoscale diaphite, where interfacial atoms comprise a substantial proportion of the entire diaphite. This scenario is expected to induce a remarkable variation in the electronic and optical property, making it easy to monitor. Indeed, synthesis of covalently-bonded diaphite proves to be very difficult; because such configuration is metastable with a positive interfacial energy calculated to be 0.36 eV $Å^{-2}$. [16] So far, extreme synthesis conditions, such as extraterrestrial impacting and high-pressure high-temperature (HPHT, typically at ≈1.0×10^{10} Pa and ≈1500 °C), are required in one-step synthesis of covalently-bonded diaphite.[8,12,17] Besides, with the help of metal catalysts (e.g., Ga and Ni) to reduce the formation barrier, a two-step method, involving diamond deposition followed by catalytic graphitization, has been reported.[13,18–20] However, in these reported diaphite, the covalently-bonded interface constitutes a small proportion compared to diamond or graphite bulk. A nanoscale diaphite dominated by a large covalently-bonded interface has not been synthesized. In this context, plasma-enhanced chemical vapor deposition (CVD) has demonstrated great potential in constructing nanoscale diamond, including nanoplatelet,[21,22] nanowire,[23] hierarchical nanostructure,[24] ultrathin nanofilm,[25] etc, through rationally adjusting the plasma parameters and tuning the interaction between plasma and carbon species.[26,27] Nevertheless, the preparation of covalently-bonded nanoscale diaphite using plasma-enhanced CVD method has rarely been reported.

In this work, we report the preparation of covalently-bonded diaphite nanoplatelets using a pillar-modified microwave plasma-enhanced CVD system. Interfacial atomic and electronic structures of diaphite nanoplatelet are investigated by transmission electron microscopy (TEM) equipped with electron energy-loss spectroscopy (EELS) and density functional theory (DFT) calculations. Significantly, cathodoluminescence (CL) spectrum verifies that the covalently-bonded diaphite exhibits a varied optical emission peak associated with the energy band structure compared to pristine diamond. Furthermore, the growth mechanism of covalently-bonded diaphite is uncovered based on elucidating the interplay between pillar-modified plasma characteristics and nanostructure evolution. This work presents a simple one-step CVD method for developing covalently-bonded nanoscale diaphite. Furthermore, the results demonstrate the potential of covalently-bonded diaphite in engineering the electronic property of diamond, endowing its promising applications in functional electronic devices.

2. Results and Discussion

2.1. Microstructure of Covalently-Bonded Diaphite

The schematic illustration for the growth of covalently-bonded diaphite by the microwave plasma-enhanced CVD is shown in **Figure 1a**. The Al_2O_3 pillar plays a vital role in the formation of diaphite. The substrate temperature (T_s) was raised up to ≈1060 °C on the pillar, much higher than ≈675 °C on the Mo stage when using identical experimental parameters. This suggests that the plasma density was greatly enhanced on the substrate surface. Figure 1b displays the surface morphology of the diaphite. Note that networked nanowalls densely cover on the bright nanoplatelets. In Figure 1c, well-characterized peaks located at 1333, 1413, and 1584 cm^{-1}, corresponding to the T_{2g} band, D band, and G band, respectively, are observed in the Raman spectrum with an excitation laser of 325 nm, suggesting the diaphite is composed of diamond, graphite, and amorphous carbon. By contrast, nanocrystalline diamond was obtained without the Al_2O_3 pillar (see Figure S1, Supporting Information). Moreover, the bottom panel in Figure 1c displays the Raman spectrum obtained with 532 nm. They are fitted based on the Ribeiro-Soares et al. report.[28] Three main peaks, lined in Lorentzians, are related to the D band (named D^A), G band (named G^A), and D' feature of the graphite. The other two broad peaks, lined in Gaussians, are designated as D^S and G^S peaks. The T_{2g} diamond signature here could not be recognized because of the small scattering cross-section for the diamond when using 532 nm laser. The G^A peak appears at 1590 cm^{-1}. The full width at half maximum is estimated to be 51 cm^{-1}, suggesting an average grain size of ≈16 nm for the graphite domains.[28] Ribeiro-Soares et al. reported that the polycrystalline graphene with an average grain of ≈17 nm exhibited a nearly ideal G^A band poisoned at ≈1579 cm^{-1}.[28,29] We here suppose that the main cause for this distinct blueshift of G^A band is the hardening of phonons induced by pressure stress and/or the doping of graphene.[30–32]

TEM investigations were conducted to reveal the microstructure. Figure 1d shows a typical nanoplatelet, in a thickness of ≈18 nm, is wrapped by the vertically aligned nanowalls. The fast Fourier transformation (FFT) pattern, corresponding the rectangle region in Figure 1e, is well in line with the diamond theoretical diffracted spots along the [011] zone axis, confirming the nanoplatelet constituted by diamond phase (see Figure 1f). Evidenced by the alternately dark and bright lamellae as well as the high-resolution TEM image in Figure S2 (Supporting Information), it is revealed that multiple twins penetrate through the diamond nanoplatelet. In addition, the carbon nanowalls composed of multilayer graphene almost perpendicularly grow on $(11\bar{1})$ tabular plane of the diamond nanoplatelet. The carbon nanowalls are designated as vertical graphite (VG) in the following. Figure 1g shows the detailed inverse Fourier-filtered image at the phase interface of the diaphite, which were derived from the area marked by the dashed rectangle in Figure S3

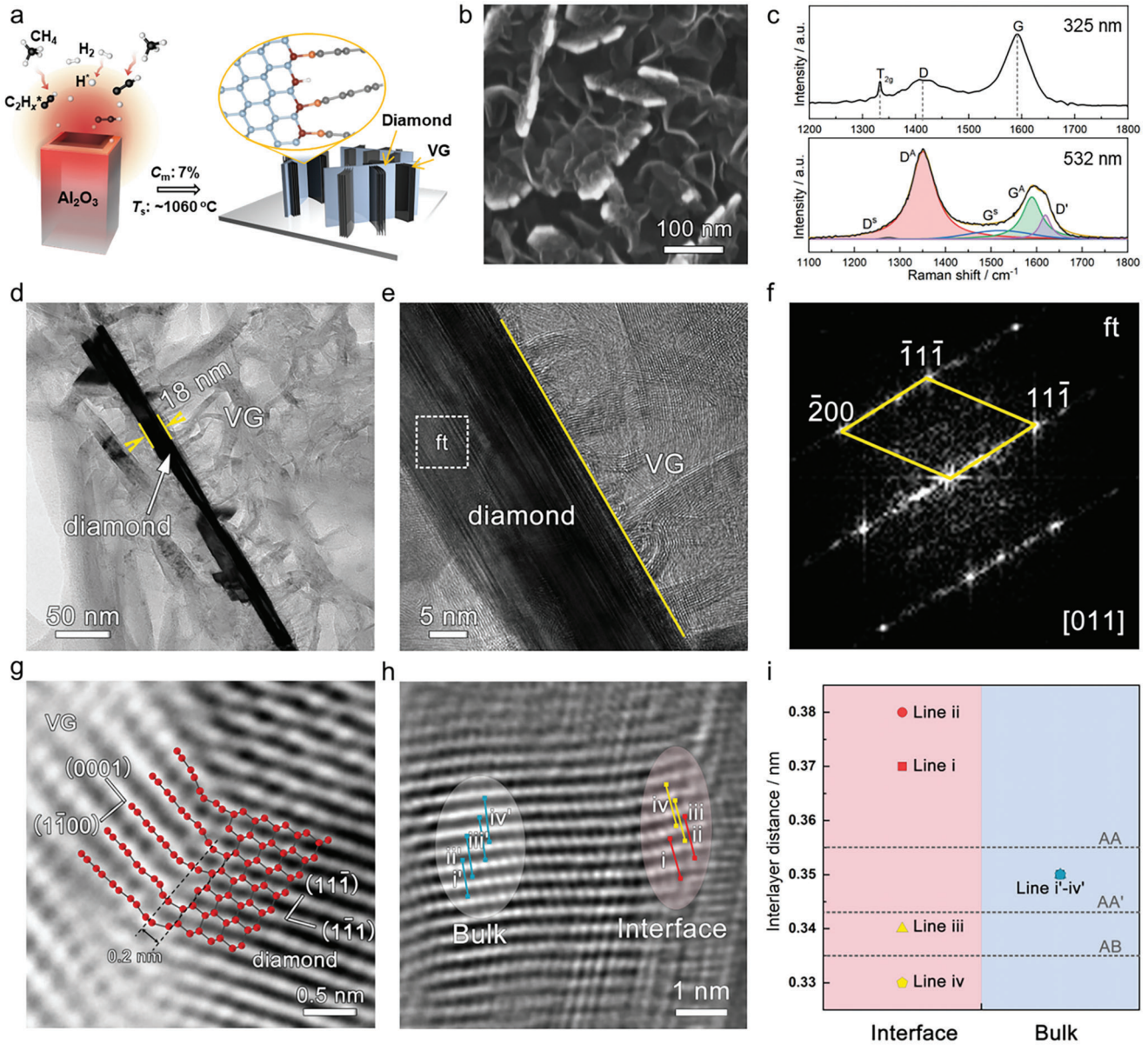

Figure 1. The preparation routine and microstructure characterizations of covalently-bonded diaphite. a) Schematic diagram illustrating the synthesis process of diaphite. b) Surface scanning electron microscopy (SEM) image of the diaphite. c) Raman spectra of the diaphite prepared with the growth time of 5 min using an excitation laser of 325 and 532 nm. d) Cross-sectional TEM image, e) high-resolution TEM image, and f) FFT pattern of the diaphite. g) Inverse Fourier-filtered interfacial image derived from the area marked by the dashed rectangle in Figure S3 (Supporting Information). h) High-resolution TEM image of the graphite layers from the interface to the bulk. i) Statistical interlayer distances corresponding to the painted lines i–iv at the interface and i"-iv" in the bulk.

(Supporting Information). The interface is running parallel both to the (11$\bar{1}$) plane of diamond and to the (1$\bar{1}$00) plane of graphite. Thus, the beam direction is the [011] of diamond, also, the [11$\bar{2}$0] of graphite. There is small inclination angle, estimated to be ≈20°, between the (1$\bar{1}$1) plane of diamond and (0001) plane of graphite. Furthermore, an interfacial atomic model is superimposed on the bright dots, which were considered as the position of the projected atomic columns. Obviously, the diamond planes are covalently bonded to the graphene layer, with three (1$\bar{1}$1) planes for two (0001) planes (3:2 registry) and a 2:2 registry. Across the diaphite interface, the distances between neighboring bright dots were measured to be 0.15–0.24 nm, which closely aligns with the reported distance between graphite and the covalently-bonded diamond (0.18–0.28 nm).[13,19] The painted graphite atoms are seen to deviate from the ideal atomic position on (0001) plane. Thus, the interlayer distances of graphite split from the theoretical values at the interface, which is further ensured by the Figure 1h. The overall high-resolution TEM image is shown in Figure S4 (Supporting Information). The intensity profiles of the indicated lines in Figure 1h are displayed in

Figure S5 (Supporting Information), and the measured interlayer values are summarized in Figure 1i. Typically, the graphite shows two groups of spacing, namely, 0.37–0.38 and 0.33–0.34 nm, at the interface, while similar spacing (0.35 nm) in the bulk. From Lee et al., the interlayer distance of graphite (0001) plane depends on the stacking order, such as 0.335 nm for AB-stacking, 0.334 nm for ABC-stacking, 0.343 nm for AA'-stacking, and 0.355 nm for AA-stacking.[33,34] However, the unique spacing, 0.37–0.38 nm, is larger by 5%–13% than these reported values. Indeed, it is the covalent crystallographic relation that causes the large deviation of interlayer distance across the interface. If the graphene layers extend from the interface, a thermodynamically stable stacking sequence (AA or turbostratic) is eventually obtained.[29,33]

2.2. Formation Mechanism of Covalently-Bonded Diaphite

To understand the plasma characteristics for the growth of diaphite, numerical simulations were carried out. Figures S6 and S7 (Supporting Information) demonstrate a comparable electric field distribution using a 3D model and a 2D model (see Note S1, Supporting Information). Thus, the 2D model was employed in the following to investigate plasma to simplify the model and promote simulation convergence. When the pillar is employed, the electric field reaches a higher value, measured to be 1.35×10^4 V m^{-1}, near the top of the pillar (see **Figure 2**a; Figure S8, Supporting Information). Compared with the nearly uniform distribution on Mo stage, electrons accumulate around the pillar (see Figure 2b). The electron density remains consistently high within a few millimeters above the pillar but decreases rapidly as one moves radially away from it. The plasma ball is elevated by the Al_2O_3 pillar in the cylinder chamber. Besides, a bit higher electron temperature is observed on the top of Al_2O_3 pillar (see Figure 2c). Figure 2d displays that the electron density reaches as high as 1.46×10^{17} m^{-3}, which is 2.7 times of that on the Mo stage. The electron temperature increases from 2.08 eV on the Mo stage to 2.68 eV atop the pillar. Since gas temperature is mainly determined by the energy transfer during electron-gas molecule collision, the higher electron density results into a much higher gas temperature measured to be ≈1500 K above the Al_2O_3 pillar (see Figure S9, Supporting Information). Furthermore, experimentally, in contrast to the blurring plasma on the Mo stage, one can distinguish a bright, sharp plasma ball concentrating around the Al_2O_3 pillar, suggesting a much higher plasma intensity than that on the Mo stage (see Figure 2e). The plasma ball is elevated axially and shrunk radially, appearing like a torch in the cylinder reactor. This corroborates the result of electron density exhibited in Figure 2b, proving the reliability of the plasma simulation. Additionally, by analyzing the Balmer atomic hydrogen emission lines at ≈655 and ≈486 nm, C_2 swan emission lines at ≈516 and ≈471 nm, it is determined that the plasma at both Mo and Al_2O_3 is predominantly composed of H and C_2 species (see Figure 2f).[35,36]

The simulations and experimental observations reveal that a high-density plasma is created on the Al_2O_3 pillar in the diaphite formation. What is the dependence of it on the diaphite evolution? At the early stage of 5 min growth, diamond nanoplatelets are sparsely emerging from the Si substrate, and VG film is not clearly seen on most nanoplatelets (see Figure 2g). The height of the diamond nanoplatelet is estimated to be ≈87 nm (see Figure 2h; Figure S10a, Supporting Information). After 8 min growth, diamond nanoplatelets surrounded by VG take into formation (see Figure 2i), and the height of the nanoplatelet is measured to ≈120 nm (see Figure 2j; Figure S10b, Supporting Information). The above microstructural transformations verify that the rapid formation of VGs on diamond surface requires the diamond nanoplatelets with sufficient height.

Taking into account the interplay between the high energy of plasma and the evolution of nanostructures, the growth mechanism of covalently-bonded diaphite is scrutinized in the following. On one hand, from Levchenko et.al., the nanostructure characteristics greatly affect the ion current distribution in the plasma sheath, meanwhile, which in turn determines the development of nanostructures.[26] During the deposition, the diamond nanoplatelet first propagates from the seed through the planar defect-facilitated growth mechanism (see Figure S2, Supporting Information).[21] Subsequently, when the height of diamond nanoplatelet approaches a critical value, the reactive ions in the plasma will be dramatically focused on the nanoplatelets, contributing to the rapid formation of VGs. The threshold value can be estimated from the sheath length. Using the electron density (1.46×10^{17} m^{-3}) and electron temperature (2.68 eV) from numerical simulations, the sheath length is calculated to be 26 μm.[27] Considering that the reported critical height of 200 nm at a sheath length of 52 μm, we could rationally assume that is ≈100 nm in the present work. This is in well consistence with the morphology variations (see Figure 2g–j). On the other hand, the formation driver of covalent diaphite interface is further explained. During CVD, the high energy of plasma possesses abundant hot electrons that excite highly energetic hydrocarbon and hydrogen species by frequent electron-heavy species collisions. These hydrocarbon species show capability to surmount the high interfacial energy barrier (0.36 eV $Å^{-2}$) and covalently bond with the diamond lattice.[16] In addition, atomic hydrogen species play a pivotal role in mostly removing the graphite carbon atoms adhering on diamond by van der Walls force, even though it is more thermodynamically favored.[37] This leads to the formation of diaphite, a robust, covalently-bonded structure between graphite and diamond. The above growth model is schematically shown in Figure 2k.

Overall, the pillar-induced high energy of plasma drives the one-step formation of covalently-bonded diaphite through CVD method. This technique requires a more facile pressure and temperature than HPHT and ensures no contamination from metal catalysts. More importantly, our CVD diaphite nanoplatelet possesses an $(11\bar{1})$ tabular surface of diamond, where (0001) graphite planes covalently connect with $(1\bar{1}1)$ diamond planes in a 3:2 and a 2:2 registry. This configuration distinctly differs from previously synthesized gradia structures using the HPHT method, where the {111} diamond planes and (0001) graphite planes are covalently bonded in a one-to-one correspondence at the interface.[8] In the meteorite and laboratory-shocked graphite samples, Péter Németh revealed the covalent bonding of graphite (0001) layers occurs at high angles to the {113} surfaces of diamond domains, without a one-to-one correspondence.[12,38] The varied terminated crystalline surface of diamond results in a slightly smaller interlayer spacing of graphite (0.3 nm) than observed herein

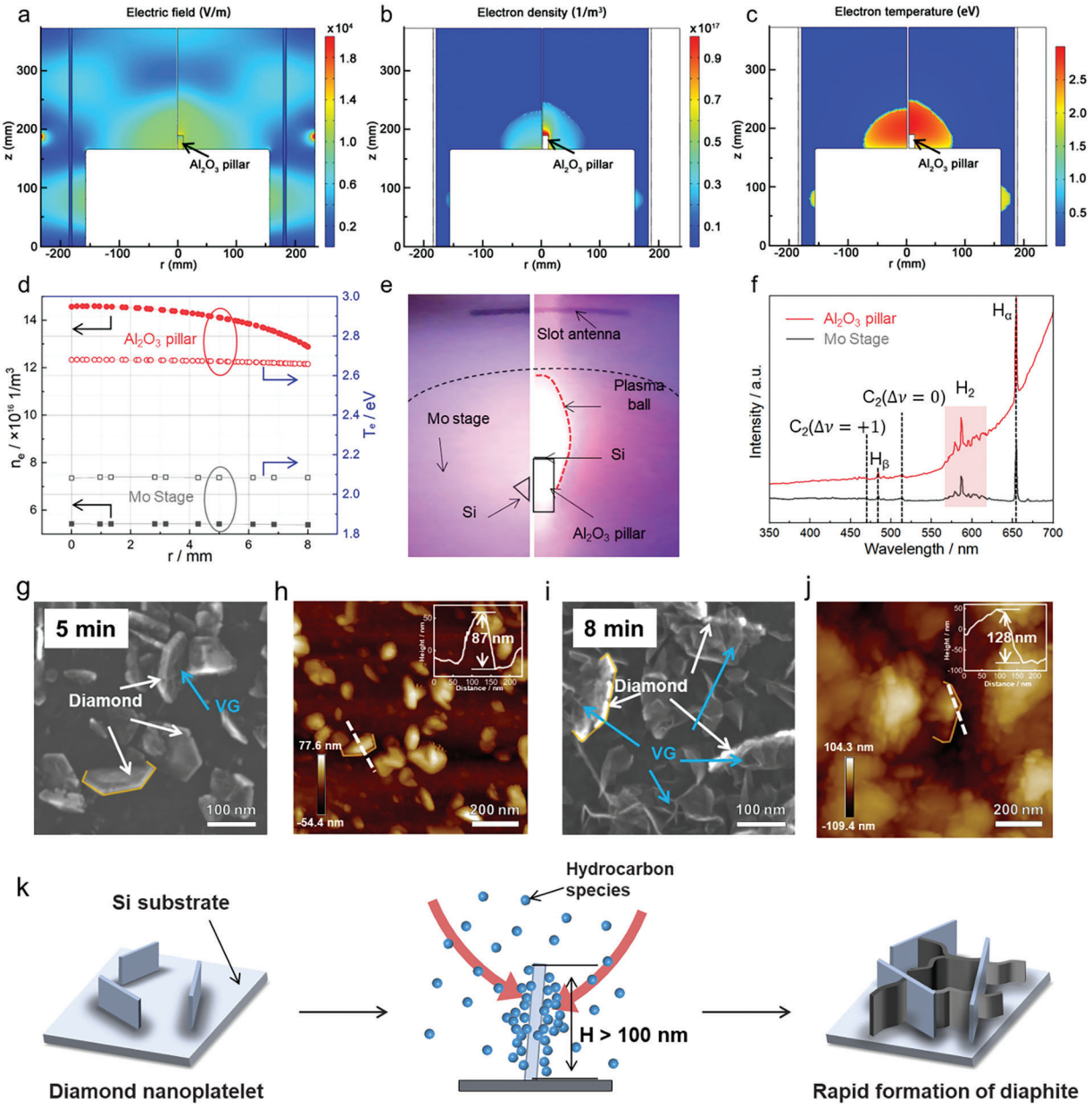

Figure 2. Growth mechanism of the covalently-bonded diaphite in CVD. a) Electric field distribution, b) electron density distribution, and c) electron temperature distribution in the cylinder resonator without (left panel) and with (right panel) the pillar in H_2 source gas. d) Comparison of the electron density profiles and electron temperature profiles along the radial line 1 mm above the top of the Mo stage and the pillar in H_2 source gas. e) Photograph images of the plasma without and with the pillar in H_2 source gas and f) optical emission spectra of the plasma without and with the pillar in H_2 source gas containing 7% CH_4. g,i) SEM morphology images and h,j) atomic force microscopy (AFM) topographies of the diaphite grown with (g,h) 5 min and (i,j) 8 min. k) Schematic growth model. The inset in (h,j) shows the height profiles corresponding to the indicated dash lines.

(0.33–0.38 nm). Meanwhile, the covalently-bonded diaphite interfaces were created on the surface of diamond plate using methods including metal catalytic etching or plasma etching.[4,13] They exhibit an analogous interface microstructure with that identified in our study. However, the diamond plate is in centimeter size, which contrasts significantly with our diaphite composed of diamond nanoplatelet in ≈18 nm thickness, covalently bonded by graphite on the sides. The diaphite nanoplatelet here possesses a significant proportion of the covalently bonded interface, which is expected to trigger a noticeable influence on the electronic properties of the diamond.

2.3. Electronic Property of Covalently-Bonded Diaphite

To access the electronic property of the covalent diaphite, micro-region CL investigations were carried out at room temperature. At the marked cross in **Figure** 3a, we recorded the corresponding

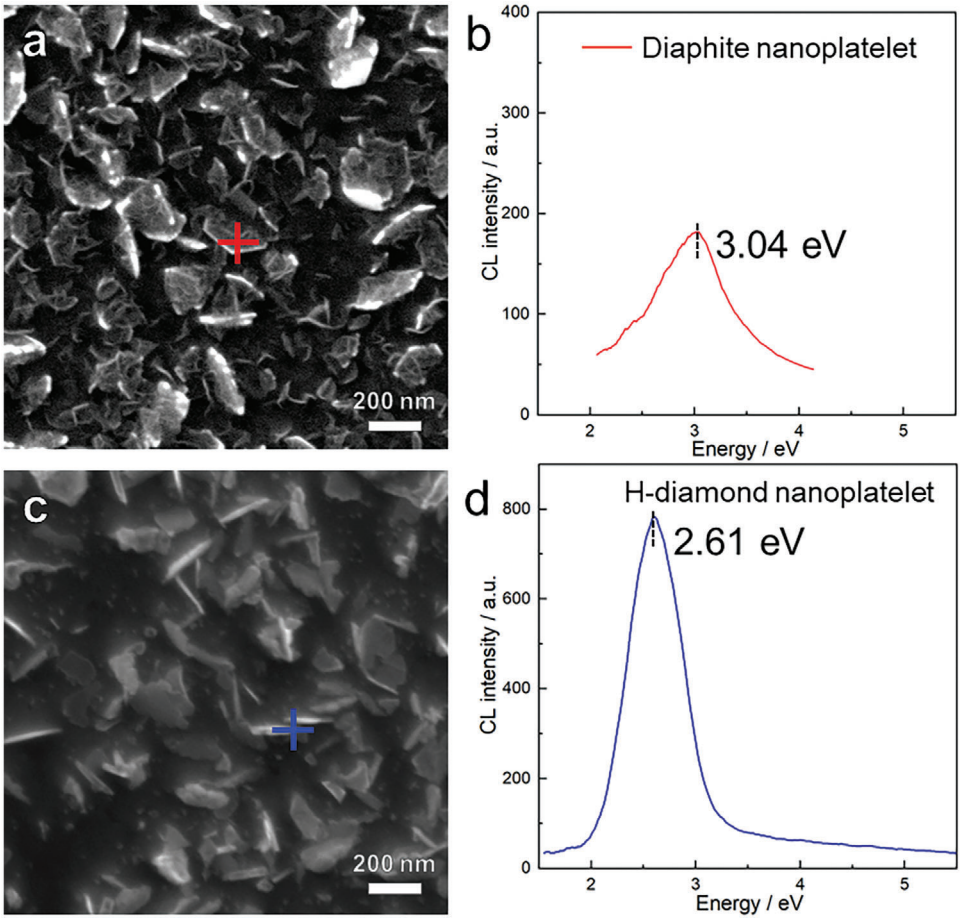

Figure 3. CL investigations on the electronic property of covalently-bonded diaphite. SEM images of a) the diaphite nanoplatelet and c) the H-diamond nanoplatelet. CL spectra were obtained at the designated points on the b) diaphite nanoplatelet and d) H-diamond nanoplatelet in panel (a) and (c).

CL spectrum of the diaphite nanoplatelet (see Figure 3b). It is seen that a dominant broad peak located at ≈3.04 eV for the diaphite, compared to the no-signal background from Si substrate (see Figure S11, Supporting Information). It is worth mentioning that the diaphite edge region displays a reduced density and broader peak compared to the center area, which may result from the microstructural variation (see Figure S12, Supporting Information). Further efforts are needed to clarify the heterogeneous CL behavior. Meanwhile, in order to clear the impart of covalently bonded graphite on the CL response, the diaphite was treated in an acid mixture consisting of H_2SO_4 and HNO_3 in a volume ratio of 3:1 at 150 °C to eliminate the surface graphite, followed by an H_2 plasma treatment to obtain H-terminated diamond (H-diamond) nanoplatelet. In Figure 3c,d, and Figure S13 (Supporting Information), the marked H-diamond nanoplatelet and clusters display distinct peaks at ≈2.61 eV, which is consistent with the previously reported range of 2.45–2.8 eV on CVD diamond film.[39] No sharp line, corresponding to the nitrogen-vacancy zero state in diamond, is observed at ≈2.16 eV.[40] Besides, the time-of-flight secondary ion mass spectrometry (ToF-SIMS) reveals the constituent profile along the depth (see Figure S14, Supporting Information). The diaphite film and Si substrate were distinguished by the Si^- signals. The C_5^- signal gradually decreases as it goes deeper into the Si. Note, the intensity of N^- and NH^- ions remain zero within both the diaphite and Si layer, indicating few nitrogen incorporation into the diamond lattice during deposition. From Dean et al, such broad peak is interpreted with the band A related to radiative transitions between trapping levels below the conduction band minimum (CBM) and the valence band itself.[41,42] These trapping levels are caused by intrinsic defects, such as vacancies and dislocations, in the diamond lattice. Notably, this peak demonstrates a blueshift of 430 meV, manifesting to a modified electronic structure compared to pristine diamond, after the surface hybridization of diamond with graphite.

To understand the origin of the modulation in electronic properties observed in diaphite, we conducted high-resolution EELS analysis at the covalently-bonded diaphite interface using aberration-corrected TEM. **Figure** 4a displays the bright-field (BF) TEM image on the left panel and the atom-resolved high-angle annual dark-field (HAADF) scanning transmission electron microscopy (STEM) image on the right panel. It is noticed that the graphite (0001) layer covalently bonds with diamond ($1\bar{1}1$) plane at the interface, as indicated by the yellow triangle. Furthermore, Figure 4b depicts the core loss spectra acquired from the corresponding regions of Figure 4a. In regions 1–5, the spectra show the $1s\rightarrow\pi^*$ transition peak at 285 eV and $1s\rightarrow\sigma^*$ transition peak at 292 eV, which are typical feature of graphite-like sp^2-carbon.[20,43]

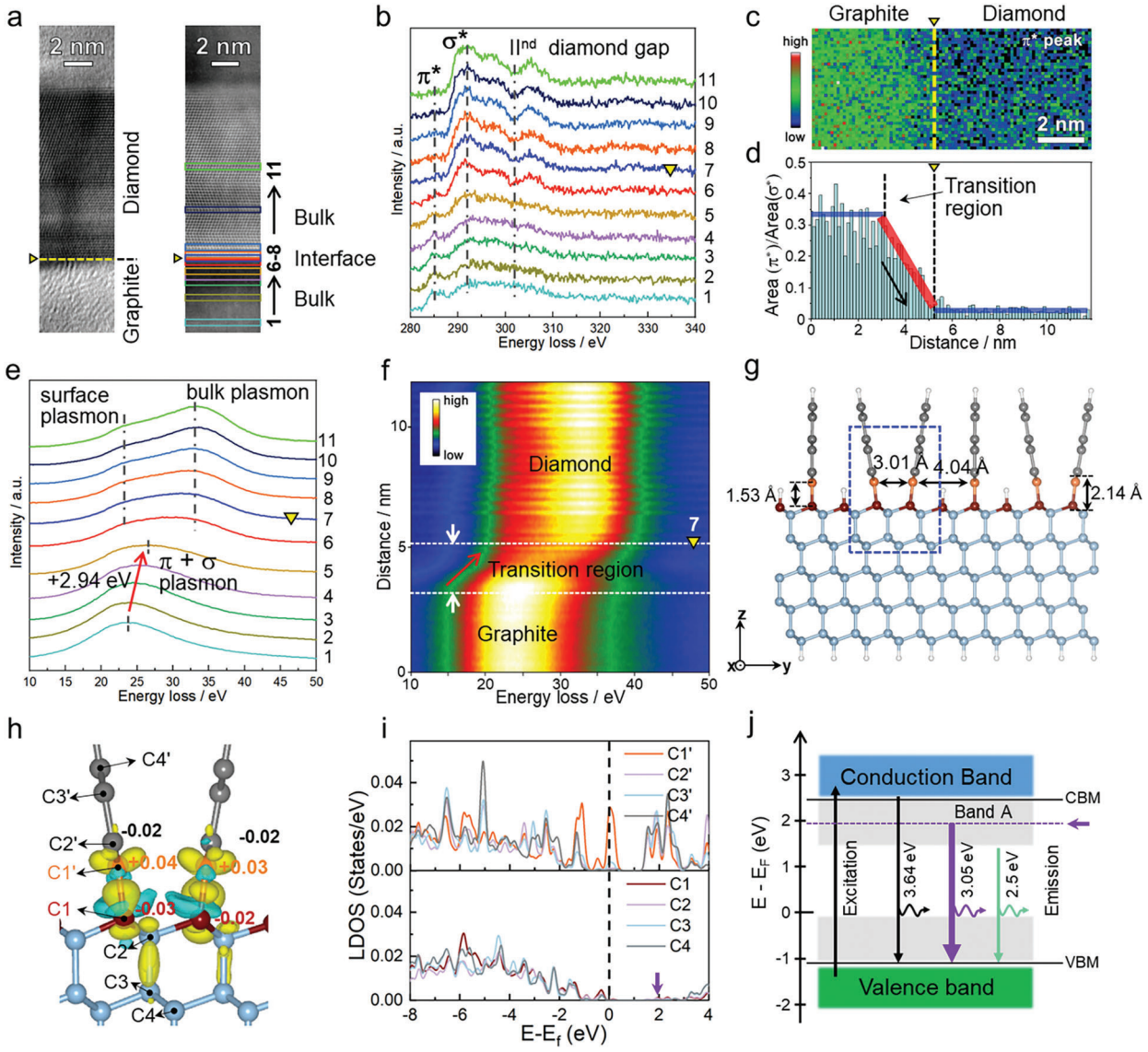

Figure 4. EELS investigations and DFT calculations on the electronic property of covalently-bonded diaphite. a) BF TEM and corresponding HAADF STEM images of the diaphite. b) Core-loss spectra acquired from corresponding regions in panel (a), c) The carbon K-edge π^* mapping signal (284–288 eV). d) Histogram of the area ratios of π^* peak to σ^* peak, estimated by performing Gaussian fitting on the core loss spectra. e) Plasmon loss spectra acquired from the corresponding regions in panel (a). f) The plasmon-loss line scan image across the interface. g) A front view of the optimized atomic diaphite model. h) Difference of charge densities at the diaphite interface. i) LDOS for the specific carbon atoms in graphite phase and diamond phase. These carbon atoms are indicated in the panel (h). j) Schematic energy diagram of the interfacial diamond segment. The diamond/graphite interfaces are indicated by yellow triangles in panel (a–f).

In regions 6–8, the spectra are dominated by a distinct σ^* peak and a large dip at 302 eV characteristic for diamond sp^3-carbon, whereas a small π^* peak could still be resolved.[44] Moving to regions 9–11, the spectra demonstrate the sp^3-carbon bond state of diamond. Figure 4c shows the intensity distribution of the π^* signal across the diamond/graphite interface. The bulk graphite region exhibits a higher π^* intensity compared to the bulk diamond region. Notably, a transition zone exists near the interface within the graphite region, which is further confirmed by the histogram of the area ratios in Figure 4d. The core loss spectra were fitted using Gaussian methodology, and the areas of π^* peak and σ^* peak were determined by integrating the Gauss curves at 285 and 292 eV, respectively.[45,46] In the bulk graphite region, the π^*-to-σ^* area ratio is estimated to be ≈0.35. However, it begins to decrease at the transition region and falls to nearly zero at the interface. This ratio remains at zero in the bulk diamond region. The transition zone near the interface indicates that the covalent diaphite possesses an interfacial area with a hybrid sp^3/sp^2-carbon bond state.

Compared with the core-loss spectra being sensitive to the valence band electrons, plasmon-loss spectra could provide more information, such as electron density in the surveyed area.[47] Figure 4e shows the plasmon loss spectra corresponding to the denoted regions in Figure 4a. The regions 1–5 show only a peak

located at ≈25 eV, which could be assigned to be the $\pi+\sigma$ oscillation amidst graphite-like sp^2-carbon.[48,49] Moving to the interface, the loss peak becomes broader and eventually splits into two characteristic peaks with energies of 33 and 23 eV, corresponding to the bulk and surface plasmons of diamond carbon, respectively.[36,48] These peaks become more outstanding in regions 9–11. Significantly, the $\pi+\sigma$ plasmon energy increases gradually from 23.67 to 26.61 eV, as one approaches the interface. It is further confirmed by the plasmon-loss line scan result in Figure 4f. As indicated by the line, the $\pi+\sigma$ peak gradually increases in the transition region near the interface. Once crossing the interface, only the dominant bulk plasmon peak could be found at 33 eV. Due to the positive correlation between the energy and the electron density, the increasing tendency discloses a higher electron density of the carbon near interfacial area.[48]

The marked deviation in the graphite interlayer distance (see Figure 1i), along with the gradual decline of π^* signals (see Figure 4c,d) as well as the increase of electron density near the interface (see Figure 4e,f), collectively serves as evidence for the existence of potent interfacial interactions in the covalently-bonded diaphite. To uncover the impact of intense interfacial interactions on the electronic properties of diaphite, we performed DFT calculations. The possible atomic model of the diaphite interface structure is constructed on the basis of the TEM images. The dangling bonds have been saturated with hydrogen atoms, which is due to the hydrogen-rich growth conditions. After structure optimization, the obtained atomic structure is presented in Figure 4g. In the interfacial region, three diamond $(1\bar{1}1)$ planes merge to two graphite planes with a spacing of 4.04 Å, and the 2:2 registration is observed to yield a spacing of 3.01 Å. The smaller interfacial interlayer spacing (3.01 Å) than the ideal value (3.35 Å) of graphite could lead to a blueshift of G^A band,[50] as observed in Figure 1c. The mass centers of nearby atoms between diamond and graphite exhibit a spacing of 2.14 Å, in well agreement with the value determined by TEM. This further confirms the covalent bonding between the diamond lattice and graphite planes. Besides, the covalent bond length is measured to be 1.53 Å between diamond and graphite, larger than that of sp^2-bonded graphite (1.42 Å) but smaller than that of sp^3-bonded diamond (1.54 Å). This suggests that the interfacial bonds are derived from both sp^2- and sp^3-hybridized orbitals, in consistent with the hybridized π^* and σ^* signals at the diaphite interface in the core-loss EELS investigations. Meanwhile, the atomic charge distribution at the diaphite interface was investigated using the Löwdin method. As shown in Figure 4h, the charge near the interface for graphite C1' atom is estimated to be +0.04 and +0.03, whereas the values for the interfacial diamond C1 atom and the next-nearest graphite C2' atom range from −0.03 to −0.02. This implies that the electron transfer occurs from the diamond phase and graphite bulk phase to the interfacial graphite carbon atom and results in a highly localized electron density near the interface, which is in well line with the plasmon-EELS results. Additionally, the electron-doped graphene contributes to a blueshift of G^A band (see Figure 1c).[32]

Significantly, charge transfer was demonstrated to play an effective role to control of the electronic states and bandgap of graphene (e.g., band shift, gap open, and close).[51,52] In our case, the electron transfer from diamond to graphite, derived from the covalently-bonded interface, also causes variations in the electronic properties of both diamond and graphite. As shown in the local density of states (LDOS) result in Figure 4i, interfacial C1' atom possesses abundant electron states across the Fermi level, even higher than those of C2′-C4′ atoms in the bulk graphite. Figure S15 (Supporting Information) reveals such unprecedented electron bands are majorly originated from p_x and p_y orbitals. Within the diamond phase, the surface C1-C2 atoms possess some local states above the valence band maximum (VBM) and below the CBM, in contrast to the bulk C3-C4 atoms. A schematic energy diagram of the interfacial diamond segment is further established in Figure 4j based on the LDOS result. The estimated ≈3.57 eV bandgap in the covalently-bonded diamond is smaller than that of the bulk diamond (5.5 eV), aligning with previous predictions for 2D diamond nanoplatelet.[53,54] The gray band near both VBM (≈−1.11 eV) and CBM (≈2.46 eV) signifies the presence of local trapping states induced by electron transfer associated with sp^3/sp^2-hybridized bonding. During the CL process, electrons are excited to the conduction band by fast incident electrons, then tend to decay to the VBM directly or undergo transition to intermediate states within the bandgap, followed by decaying to the VBM.[55] Photons are emitted during the above decaying process. Because the energy band A near the CBM extends from ≈1.39 to ≈2.53 eV, the luminescence reveals a photon energy range from ≈2.5 to ≈3.64 eV, which is almost consistent with the recorded CL spectrum in Figure 3. Meanwhile, as indicated by pink arrows in Figure 4i,j, the interfacial diamond segment possesses high local density of states at ≈1.94 eV, thereby contributing to a prominent peak at ≈3.05 eV. It should be underlined that the profound variation in the electronic structure observed here was not reported on a graphite-modified bulk diamond plate with an analogous covalently-bonding interface.[4] We suggest that nanoscale diamond, rather than centimeter diamond, covalently bonded with graphite on surfaces is another key factor to achieving the diamond electronic property modulation because interfacial atoms constitute a significant proportion and play a crucial role in imparting the electronic properties of the nanoscale diaphite. Overall, the strong interfacial interactions within the diaphite nanoplatelet, arising from intense covalently bonding, engineer the electronic and optical property of diamond.

Diamond and graphite covalently hybridize and give rise to an emerging class of elemental carbon materials known as diaphite, which offers unprecedented features to be leveraged into vast technological applications. As experimentally deemed previously, covalently-bonded diaphite structure shows improved fracture resistance while retaining the superhard nature of the diamond,[8] making it highly significant in the field of abrasive protection coatings. Moreover, we herein demonstrated such engineered electronic properties endow covalently-bonded diaphite reduced bandgap compared to diamond. This modification is exciting for advanced diamond-related electronic devices. Note, very recently, diode-like characteristics have already been monitored in I–V plots when semiconducting covalently-bonded diaphite assembles with conducting graphite into a junction.[56] This junction was created in the bulk diamond with superior thermal dissipation capacities, thus enabling a potential application in high-power, high-frequency, and densely integrated circuits. Besides, DFT calculations illustrated that the strain-induced shift of the covalent interface can effectively tune the electronic

property from insulator to semiconductor and conductor,[57] indicating that the diaphite might be used in microelectronic mechanical systems. Further applications are suggested by our prior research on the exceptional electrical double-layer capacitance of the expanded vertical graphene/diamond film originating from the covalently-bonded diaphite precursor.[58] The ultrahigh mechanical robustness of covalent bonds inhibits the detachment of graphene from diamond nanoplatelets, thereby ensuring the high structural stability during the preparation stage and electrochemical utilization. Nevertheless, the intriguing diaphite material is still in the initial stages. Tremendous efforts are still required in both the preparation of large-sized diaphite material and the exploration of its potential applications.

3. Conclusion

In summary, covalently-bonded diaphite nanoplatelet was prepared by pillar-modified microwave plasma enhanced CVD and demonstrated an altered electronic property compared to the H-diamond. The diaphite is composed of diamond nanoplatelet covalently bonded with graphene layers on surfaces, featuring an interface structure with diamond $(1\bar{1}1)$ planes merging to graphite (0001) planes in a 3:2 and a 2:2 registry. Plasma simulation and experimental investigations verify that the pillar induces high energy of plasma, which constrains hydrocarbon species toward the diamond nanoplatelets as well as endows them with the energy to overcome the interfacial energy barrier, eventually, facilitating the formation of covalently-bonded diaphite by CVD. Significantly, the strong covalent bonding induces the noticeable deviation of the graphite interlayer distance, an sp^3/sp^2-hybridized carbon area, a highly localized electron density area, and an engineered diamond electronic structure at the diaphite interface. EELS and DFT calculations reveal electron transfers from diamond to graphite through the covalently-bonded interface, creating local trapping states above the VBM and below the CBM within the bandgap in the near-interface layer of diamond. The energy band A near the CBM possesses an energy range from 1.39 to 2.53 eV, with a high local density of states at 1.94 eV. As a result of radiative transitions from band A to the VBM, the covalently-bonded diaphite nanoplatelet exhibits luminescence ranging from 2.5 to 3.64 eV, featuring a prominent peak at 3.04 eV and a blueshift of 430 meV compared to the H-diamond. This work not only promises the great potential of covalently-bonded diaphite in modulating the electronic property of diamond but also introduces a novel CVD method for fabricating the diaphite, thus, opening up new prospects in the "extreme" semiconductor application of diamond.

4. Experimental Section

Preparation of Covalently-Bonded Diaphite: The covalently-bonded diaphite was prepared by growing on n-type Si (100) substrates (13 × 14 mm^2, 525 µm thickness, and 8–20 mΩ·cm resistivity) using a 915 MHz microwave plasma-enhanced CVD setup (Iplas, Cyrannus). Before deposition, the cleaned Si substrates were sonicated for 30 min in the diamond suspension (0.025 w/v%, NanoCarbon Research Institute, Ltd., NanoAmando Colloid) to enhance nucleation. Deposition was conducted at a plasma power of 6 kW, a chamber pressure of ≈30 mbar, a hydrogen flow rate of 400 sccm, and a methane flow rate of 28 sccm. Notably, an Al_2O_3 pillar, with a height of 24 mm, was placed on the molybdenum holder to support the Si substrate into the plasma ball. The typical T_s was estimated to be ≈1060 °C by an infrared pyrometer.

Morphological and Microstructural Characterizations: The surface and cross-sectional morphology was characterized by using a field-emission SEM (Hitachi, SU-70). The surface height profiles were recorded by AFM (Bruker, Innova) using a probe tip (OLTESPA-R3, Bruker). The carbon phases were investigated by Raman spectroscopy (Horiba, Labram HR Evolution instrument), employing a 325 nm laser with a 2400 lines mm^{-1} grating and a 532 nm laser with an 1800 lines mm^{-1} grating. Single crystal silicon is used as a reference in the calibration of Raman instruments and has a well-defined Raman band with maxima at 520.7 cm^{-1}. The microstructure, especially at the diamond/graphite phase interface, was examined by TEM (FEI, Talos F200X) operating at 200 kV. Besides, to reveal the chemical bond properties, EELS was performed across the diaphite interface in DualEELS mode, where the energy loss region from −29 to 278 eV and from 240 to 548 eV were simultaneously acquired by the aberration-corrected STEM (FEI Titan Cubed Themis G2 300) equipped with an EELS system (Gatan Continuum 1065). The sample was scanned with a spatial step of 0.13 nm, an energy dispersion of 0.15 eV, an acquisition time of 0.0025 s, and a collection semi-angle of 100 mrad. The CL spectra of covalently-bonded diaphite were measured in a field-emission SEM (Hitachi, SU-70) equipped with a CL spectrometer (Horiba, MP-32S). The acquired data underwent a smoothing process before presentation. ToF-SIMS was conducted on an ION-TOF GmbH system (ToF-SIMS 5). A Cs ion gun operating at 1 keV and 40 nA current was employed to sputter an area of 300 × 300 $µm^2$. Meanwhile, a Bi1 ion gun, operating at 30 keV and with a current of 1 pA, was used to analyze the constituents over an area of 100 × 100 $µm^2$.

Density Functional Theory Calculations: DFT calculations were carried out using a hybrid Gaussian/Plane-Wave scheme (GPW)-based method CP2K code (http://www.cp2k.org) with the Quickstep module. The core electrons and nuclei were represented with the GTH-PBE pseudopotential. The wave functions were expanded in optimized double-ζ Gaussian basis sets and the plane waves were expanded with a cut-off energy of 400 Rydberg. For carbon-based materials, the DFT-D3 method was applied for dispersion correction. A big supercell of 624 atoms (544 C atoms and 80 H atoms) for the diaphite structure with the parameter a = 10.08 Å, b = 21.08 Å was constructed. The vacuum layer was settled to 30 Å to avoid interaction between the slabs. For geometry optimization, the total energy converge was below 1.0E-06 in inner SCF steps and the force converge was 4.5E-04. For electronic structure, the atom point charge is calculated using the Löwdin method. The charge density difference at the interface and LDOS of each atom were analyzed and illustrated by the Multiwfn[59] and Vesta software.

Numerical Simulations: To investigate the effect of the Al_2O_3 pillar on plasma, the simulations of the microwave plasma-enhanced CVD system were carried out. A 2D axisymmetric model was constructed based on the Cyrannus reactor, as displayed in Figure S6 (Supporting Information). During the deposition of covalently-bonded diaphite, the microwave passed through an annular resonator, then into the cylinder resonator via slot antenna. Finally, the plasma was ignited and maintained in the gas domain isolated by a quartz window. In a typical simulation, the electric field distribution inside the resonant cavity was first acquired using the 3D model, then, the electric field vectors along the microwave inlet port were regarded as initial values to excite the plasma in the 2D model. The Maxwell's equations were used to solve the microwave electric field (E) distribution, which then determined the electron number density (n_e) and electron temperature (T_e) on basis of the Füner's and Yamada's empirical model.[60–62] Furthermore, the gas temperature (T_g) distribution was examined by solving the energy conservation equation, accounting for the energy transfer from hot electrons to neutral gas molecules during the collisions. The detailed numerical simulation method is explained in Note S2 (Supporting Information).

Supporting Information

Supporting Information is available from the Wiley Online Library or from the author.

Acknowledgements

This work was funded by the National Natural Science Foundation of China (Grant No. 52202054 and 51202257), the IMR Innovation Fund (Grant No. 2021-PY14), and the Technical Innovation Project for Functional Development of Instruments and Equipment of the Chinese Academy of Sciences (No. sjzx-gnkf-202203). The authors thank Prof. Xingqiu Chen, Junnan Chen, Ye Tian, Guanglei Cui, and Wei Bao for discussions and assistance.

Open access funding enabled and organized by Projekt DEAL.

Conflict of Interest

The authors declare no conflict of interest.

Data Availability Statement

The data that support the findings of this study are available from the corresponding author upon reasonable request.

Keywords

chemical vapor deposition, covalently-bonded interface, diaphite, electronic property, gradia

Received: January 31, 2024
Revised: March 20, 2024
Published online:

[1] C. Dang, J. P. Chou, B. Dai, C. T. Chou, Y. Yang, R. Fan, W. Lin, F. Meng, A. Hu, J. Zhu, J. Han, A. M. Minor, J. Li, Y. Lu, *Science* **2021**, *371*, 76.
[2] C. Dang, A. Lu, H. Wang, H. Zhang, Y. Lu, *J. Semicond.* **2022**, *43*, 021801.
[3] H. Yang, Y. Ma, Y. Dai, *Funct. Diamond* **2022**, *1*, 150.
[4] K. P. S. S. Hembram, S. Lee, H. Im, H. Ju, S.-H. Jeong, J.-K. Lee, *Mater. Horiz.* **2020**, *7*, 470.
[5] X. Yan, Y. Jiang, B. Yang, S. Ma, T. Yao, A. Tao, C. Chen, X. Ma, H. Ye, *Carbon* **2022**, *200*, 483.
[6] Z. Shi, M. Dao, E. Tsymbalov, A. Shapeev, J. Li, S. Suresh, *Proc. Natl. Acad. Sci. U. S. A.* **2020**, *117*, 24634.
[7] C. Dang, A. Lu, H. Wang, L. Yang, X. Li, H. Zhang, Y. Lu, *Extreme Mech. Lett.* **2023**, *58*, 101931.
[8] K. Luo, B. Liu, W. Hu, X. Dong, Y. Wang, Q. Huang, Y. Gao, L. Sun, Z. Zhao, Y. Wu, Y. Zhang, M. Ma, X.-F. Zhou, J. He, D. Yu, Z. Liu, B. Xu, Y. Tian, *Nature* **2022**, *607*, 486.
[9] J. Kanasaki, E. Inami, K. Tanimura, H. Ohnishi, K. Nasu, *Phys. Rev. Lett.* **2009**, *102*, 087402.
[10] H. Ohnishi, K. Nasu, *Phys. Rev. B* **2009**, *80*, 014112.
[11] P. Nemeth, K. McColl, L. A. J. Garvie, C. G. Salzmann, M. Murri, P. F. McMillan, *Nat. Mater.* **2020**, *19*, 1126.
[12] P. Nemeth, K. McColl, R. L. Smith, M. Murri, L. A. J. Garvie, M. Alvaro, B. Pecz, A. P. Jones, F. Cora, C. G. Salzmann, P. F. McMillan, *Nano Lett.* **2020**, *20*, 3611.
[13] B. Shen, Z. Ji, Q. Lin, P. Gong, N. Xuan, S. Chen, H. Liu, Z. Huang, T. Xiao, Z. Sun, *Chem. Mater.* **2022**, *34*, 3941.
[14] X. Yan, Y. Jiang, Q. Jin, T. Yao, W. Wang, A. Tao, C. Gao, X. Li, C. Chen, H. Ye, X. L. Ma, *Nat. Commun.* **2023**, *14*, 2788.
[15] V. Petrakova, A. Taylor, I. Kratochvilova, F. Fendrych, J. Vacik, J. Kucka, J. Stursa, P. Cigler, M. Ledvina, A. Fiserova, P. Kneppo, M. Nesladek, *Adv. Funct. Mater.* **2012**, *22*, 812.
[16] S.-c. Zhu, X.-z. Yan, J. Liu, A. R. Oganov, Q. Zhu, *Matter* **2020**, *3*, 864.
[17] X. Yang, J. Dong, M. Yao, K. Hu, H. Sun, R. Liu, C.-X. Shan, B. Liu, *Carbon* **2021**, *172*, 138.
[18] S. Chen, Q. Lin, Z. Ji, Z. Sun, B. Shen, *Carbon* **2023**, *201*, 390.
[19] S. Tulic, T. Waitz, M. Caplovicova, G. Habler, M. Varga, M. Kotlar, V. Vretenar, O. Romanyuk, A. Kromka, B. Rezek, V. Skakalova, *ACS Nano* **2019**, *13*, 4621.
[20] S. Tulic, T. Waitz, M. Caplovicova, G. Habler, V. Vretenar, T. Susi, V. Skakalova, *Carbon* **2021**, *185*, 300.
[21] Z. F. Zhai, C. Y. Zhang, R. W. Xie, B. Chen, Z. W. Zheng, L. S. Liu, B. Yang, D. Shi, X. Jiang, N. Huang, *Cryst. Growth Des.* **2023**, *23*, 1528.
[22] S. Wang, X. Ji, Y. Ao, J. Yu, *Nanoscale* **2018**, *10*, 2812.
[23] I. Vlasov, O. I. Lebedev, V. G. Ralchenko, E. Goovaerts, G. Bertoni, G. Van Tendeloo, V. I. Konov, *Adv. Mater.* **2007**, *19*, 4058.
[24] Z. F. Zhai, N. Huang, B. Yang, L. S. Liu, H. N. Li, J. N. Chen, B. S. Zhang, X. Jiang, *ACS Appl. Mater. Interfaces* **2020**, *12*, 8522.
[25] S. Handschuh-Wang, T. Wang, Y. Tang, *Small* **2021**, *17*, 2007529.
[26] I. Levchenko, K. Ostrikov, *J. Phys. D: Appl. Phys.* **2007**, *40*, 2308.
[27] H. Zhuang, L. Zhang, R. Fuchs, T. Staedler, X. Jiang, *Sci. Rep.* **2013**, *3*, 2427.
[28] J. Ribeiro-Soares, M. E. Oliveros, C. Garin, M. V. David, L. G. P. Martins, C. A. Almeida, E. H. Martins-Ferreira, K. Takai, T. Enoki, R. Magalhaes-Paniago, A. Malachias, A. Jorio, B. S. Archanjo, C. A. Achete, L. G. Cancado, *Carbon* **2015**, *95*, 646.
[29] L. M. Malard, M. A. Pimenta, G. Dresselhaus, M. S. Dresselhaus, *Phys. Rep.* **2009**, *473*, 51.
[30] Z. Tao, J. Du, Z. Qi, K. Ni, S. Jiang, Y. Zhu, *Appl. Phys. Lett.* **2020**, *116*, 133101.
[31] L. G. P. Martins, M. J. S. Matos, A. R. Paschoal, P. T. C. Freire, N. F. Andrade, A. L. Aguiar, J. Kong, B. R. A. Neves, A. B. de Oliveira, M. S. C. Mazzoni, A. G. S. Filho, L. G. Cançado, *Nat. Commun.* **2017**, *8*, 96.
[32] A. Das, S. Pisana, B. Chakraborty, S. Piscanec, S. K. Saha, U. V. Waghmare, K. S. Novoselov, H. R. Krishnamurthy, A. K. Geim, A. C. Ferrari, A. K. Sood, *Nat. Nanotechnol.* **2008**, *3*, 210.
[33] J. K. Lee, S. C. Lee, J. P. Ahn, S. C. Kim, J. I. Wilson, P. John, *J. Chem. Phys.* **2008**, *129*, 234709.
[34] J. C. Charlier, X. Gonze, J. P. Michenaud, *Carbon* **1994**, *32*, 289.
[35] E. V. Bushuev, V. Y. Yurov, A. P. Bolshakov, V. G. Ralchenko, A. A. Khomich, I. A. Antonova, E. E. Ashkinazi, V. A. Shershulin, V. P. Pashinin, V. I. Konov, *Diamond Relat. Mater.* **2017**, *72*, 61.
[36] K. J. Sankaran, C. J. Yeh, P. Y. Hsieh, P. Pobedinskas, S. Kunuku, K. C. Leou, N. H. Tai, I. N. Lin, K. Haenen, *ACS Appl. Mater. Interfaces* **2019**, *11*, 25388.
[37] Y. Ma, Y. Dai, M. Guo, B. Huang, *Phys. Rev. B* **2012**, *85*, 235448.
[38] P. Németh, K. McColl, L. A. J. Garvie, C. G. Salzmann, C. J. Pickard, F. Corà, R. L. Smith, M. Mezouar, C. A. Howard, P. F. McMillan, *Diamond Relat. Mater.* **2021**, *119*, 108573.
[39] H. Kawarada, K. Nishimura, T. Ito, J. Suzuki, K. S. Mar, Y. Yokota, A. Hiraki, *Jpn. J. Appl. Phys.* **1988**, *27*, L683.
[40] M. Solà-Garcia, S. Meuret, T. Coenen, A. Polman, *ACS Photonics* **2020**, *7*, 232.
[41] J. F. Prins, *Diamond Relat. Mater.* **1996**, *5*, 907.
[42] P. J. Dean, *Phys. Rev.* **1965**, *139*, A588.
[43] I. Palacio, A. Celis, M. N. Nair, A. Gloter, A. Zobelli, M. Sicot, D. Malterre, M. S. Nevius, W. A. de Heer, C. Berger, E. H. Conrad, A. Taleb-Ibrahimi, A. Tejeda, *Nano Lett.* **2015**, *15*, 182.
[44] J. F. Morar, F. J. Himpsel, G. Hollinger, G. Hughes, J. L. Jordan, *Phys. Rev. Lett.* **1985**, *54*, 1960.
[45] J. O. Mueller, D. S. Su, U. Wild, R. Schloegl, *Phys. Chem. Chem. Phys.* **2007**, *9*, 4018.

[46] A. J. Papworth, C. J. Kiely, A. P. Burden, S. R. P. Silva, G. A. J. Amaratunga, *Phys. Rev. B* **2000**, *62*, 12628.
[47] S. Prawer, J. L. Peng, J. O. Orwa, J. C. McCallum, D. N. Jamieson, L. A. Bursill, *Phys. Rev. B* **2000**, *62*, R16360.
[48] P. Kovarik, E. B. D. Bourdon, R. H. Prince, *Phys. Rev. B* **1993**, *48*, 12123.
[49] F. Carbone, B. Barwick, O.-H. Kwon, H. S. Park, J. S. Baskin, A. H. Zewail, *Chem. Phys. Lett.* **2009**, *468*, 107.
[50] J. Nicolle, D. Machon, P. Poncharal, O. Pierre-Louis, A. San-Miguel, *Nano Lett.* **2011**, *11*, 3564.
[51] T. Ohta, A. Bostwick, T. Seyller, K. Horn, E. Rotenberg, *Science* **2006**, *313*, 951.
[52] B. Zribi, A.-M. Haghiri-Gosnet, A. Bendounan, A. Ouerghi, H. Korri-Youssoufi, *Carbon* **2019**, *153*, 557.
[53] P. B. Sorokin, B. I. Yakobson, *Nano Lett.* **2021**, *21*, 5475.
[54] L. Y. Zhu, H. Hu, Q. A. Chen, S. D. Wang, J. L. Wang, F. Ding, *Nanotechnology* **2011**, *22*, 185202.
[55] T. Sun, Y. Li, Y. Liu, B. Deng, C. Liao, Y. Zhu, *Encyclopedia of Nanomaterials*, (Eds: Y. Yin, Y. Lu, Y. Xia), Elsevier, Oxford, United Kingdom **2023**, Vol. *2*, pp 183.
[56] P. S. Salter, M. P. Villar, F. Lloret, D. F. Reyes, M. Krueger, C. S. Henderson, D. Araujo, R. B. Jackman, *ACS Nano* **2024**, *18*, 2861.
[57] B. Yang, Y. Su, Z. Wang, L. Zhao, N. Hu, *Mater. Today Phys.* **2022**, *28*, 100879.
[58] B. Chen, Z. Zhai, N. Huang, C. Zhang, S. Yu, L. Liu, B. Yang, X. Jiang, N. Yang, *Adv. Energy Mater.* **2023**, *13*, 2300716.
[59] T. Lu, F. Chen, *J. Comput. Chem.* **2012**, *33*, 580.
[60] M. Funer, C. Wild, P. Koidl, *Surf. Coat. Technol.* **1995**, *74*, 221.
[61] G. Shivkumar, S. S. Tholeti, M. A. Alrefae, T. S. Fisher, A. A. Alexeenko, *J. Appl. Phys.* **2016**, *119*, 113301.
[62] H. Yamada, A. Chayahara, Y. Mokuno, *J. Appl. Phys.* **2007**, *101*, 063302.